Thin reaction zone and distributed reaction zone regimes in turbulent premixed methane/air flames

Scalar distributions and correlations

Zhou, Bo; Brackmann, Christian; Wang, Zhenkan; Li, Zhongshan; Richter, Mattias; Aldén, Marcus; Bai, Xue Song

Published in:
Combustion and Flame

DOI:
10.1016/j.combustflame.2016.06.016

2017

Document Version:
Peer reviewed version (aka post-print)

This is the peer review version of the following article: B. Zhou, C. Brackmann, Z. K. Wang, Z. S. Li, M. Richter, M. Alden, and X. S. Bai, "Thin reaction zone and distributed reaction zone regimes in turbulent premixed methane/air flames: Scalar distributions and correlations," Combust Flame **175**, 220-236 (2017), which has been published in final form at DOI:10.1016/j.combustflame.2016.06.016

Thin reaction zone and distributed reaction zone regimes in turbulent premixed methane/air flames: scalar distributions and correlations

Bo Zhou[1], Christian Brackmann[1], Zhenkan Wang[1], Zhongshan Li[1], Mattias Richter[1], Marcus Aldén[1], Xue-Song Bai[2]

[1]*Division of Combustion Physics, Lund University, P.O. Box 118, S221 00, Lund, Sweden*

[2]*Department of Energy Science, Lund University, P.O. Box 118, S221 00, Lund, Sweden*

**Email: marcus.alden@forbrf.lth.se*

Submitted to the Special Issue of Combustion and Flame dedicated to N. Peters

Abstract

A series of premixed turbulent methane/air jet flames in the thin reaction zone (TRZ) and distributed reaction zone (DRZ) regimes were studied using simultaneous three-scalar high-resolution imaging measurements, including HCO/OH/CH_2O, CH/OH/CH_2O, T/OH/CH_2O and T/CH/OH/. These scalar fields offer a possibility of revisiting the structures of turbulent premixed flames in different combustion regimes. In particular, CH_2O provides a measure of the preheat zone, CH/HCO a measure of the inner layer of the reaction zone, and OH a measure of the oxidation zone. Scalar correlations are analyzed on both single-shot and statistical basis, and resolvable correlated structures of ~100 μm between scalars are captured. With increasing turbulence intensity, it is shown that the preheat zone and the inner layer of the reaction zone become gradually broadened/distributed, and the correlation between HCO and $[OH]_{LIF}\times[CH_2O]_{LIF}$ decreases. A transition from the TRZ regime to the DRZ regime is found around Karlovitz number of 70 – 100, consistent with the theoretical result of Peters. The physical and chemical effects on the broadening of the flame are investigated. In the TRZ regime the inner layer marker CH and HCO remains thin in general; however, effect of eddy folding combined with the effect of flame stretch can give rise to broadening of the inner layer. As a result, there is a significant probability of finding CH and HCO at rather low temperatures even in the TRZ regime. In the DRZ regime, the broadening of CH and HCO are shown to be mainly a result of local reactions facilitated by rapid turbulent transport of radicals and

intermediate reactants in the upstream of the reaction paths. Differential diffusion is expected to have an important effect in the DRZ regime, as H radicals seemingly play a more important role than OH radicals.

Key words: multi-scalar imaging; scalar correlation; regime diagram; thin reaction zone regime; distributed reaction zone regime; turbulent premixed flame structure; flame/turbulence interaction

1. Introduction

Being motivated by both industrial applications and fundamental scientific enquiries, studies of premixed turbulent combustion have attracted an increasing attention in the past decades. Of paramount importance among these studies is the work towards understanding the interaction between turbulence and flame, which is classified by a variety of combustion regime diagrams that describe the different modes of turbulent premixed flames [1-4]. According to the regime diagram, a key parameter, the so-called Karlovitz number (Ka), is employed which is defined as the ratio between the chemical reaction time associated with the flame and the smallest time scale of turbulence, i.e., the Kolmogorov time. Under the low-intensity and large-scale turbulence condition, i.e., Ka<1, the length scales of turbulence eddies are larger than the flame thickness; turbulence can wrinkle the flame while not able to modify the preheat and reaction zone structure. The flame propagates as a thin reacting layer separating the reactants and the products, and segments of the wrinkled flame can be considered as a laminar flamelet [4-6]. Peters extended the flamelet concept to the thin reaction zone (TRZ) regime [4] in which the smallest turbulence scale (the Kolmogorov scale) becomes comparable to the flame thickness while still larger than the inner layer thickness of the reaction zone. Peters [4] argued that the flamelet concept remains valid in the TRZ regime, in which the inner layer of the reaction zone stays thin and intact, although the preheat zone can be broadened by the small eddies of comparable sizes to that of the preheat zone. Peters' TRZ regime is supported by a large body of numerical and experimental studies [7-13], while it has also been shown that turbulent burning velocity may not correlate with the flame surface area for flames in the TRZ regime, which implies some limitations of the flamelet model [14, 15].

An essentially different scenario can possibly be encountered in a so-called distributed reaction zone (DRZ) regime in which the Karlovitz number is high (typically Ka>100 [4]). In this regime, it is hypothesized that the Kolmogorov scale can become smaller than the inner layer of the reaction zone so that the entire structure of the reaction zone could be substantially distorted by small-eddy penetration. As a possible consequence, the reaction zone could be broadened and/or distributed, resulting in a combustion mode fundamentally distinct from that of a laminar flamelet. However, whether or not this combustion mode (i.e. distributed reactions) can be realized through rapid turbulence mixing has been questioned due to the lack of conclusive experimental evidence of distributed reaction zones or significant reaction zone broadening [16]. Driscoll suggested that a direct experimental evidence of distributed reactions in hydrocarbon flames could be a set of single-shot images that show the CH/HCO layer to be significantly broadened/distributed in space [16]. This is because the CH and HCO radicals are formed through reactions associated with the major heat release in hydrocarbon flames [17, 18] and are extremely short-lived, which prohibits them from being transported an appreciable distance from where they are produced. Therefore, a distributed CH/HCO layer is a direct reflection of distributed reactions responsible for CH and HCO production.

It is noted that a number of work has claimed combustion with distributed reactions through various other experimental observations such as vitiated thermal gradients [19, 20], absence of flame chemiluminescence [21] or a rapid change of the minimum ignition energy with increasing turbulence intensity [22]. However, these observations alone do not necessarily indicate distributed reactions as the associated reactive species in the reaction zone were not reported.

Recently, we demonstrated that distributed reactions characterized by CH and HCO can be realized in a turbulent methane/air jet flame by varying the jet speed and equivalence ratio [23, 24], and in low swirl flames [25] by dilution from ambient air. In this paper we focus on the following two research questions: (1) the physical and chemical reasons behind the broadening of the reaction zones; (2) the impact of turbulence-flame interaction on the fields of various key scalars and the correlations among the scalars for flames in the TRZ and DRZ regimes. To reveal the structures of different reaction layers, reactive scalars of OH (oxidation and post-flame zone markers), CH_2O (preheat zone marker [26]), CH and HCO (inner layer reaction zone markers [17]) are selected and measured using planar laser-induced fluorescence (PLIF) together with temperature (T) field using Rayleigh scattering thermometry (RST). Four sets of simultaneous high-resolution three-scalar imaging measurements were performed, which include combinations of HCO/OH/CH_2O, CH/OH/CH_2O, T/OH/CH_2O and T/CH/OH. Instantaneous structures of reactive scalars (i.e. OH, CH_2O, CH and HCO) and temperature (T) are compared together with their derivatives, i.e. two-dimensional (qualitative) OH gradient ($|\nabla[OH]|_{2D}$) and two-dimensional temperature gradient ($|\nabla[T]|_{2D}$) as well as products of OH and CH_2O, of OH and CH, and of OH and HCO, which qualitatively measure the rates of the associated reactions. In particular, it has been shown that the HCO concentration is proportional to its production rate that has an excellent spatio-temporal correlation with peak heat release rate (HRR) in laminar methane/air flames [17, 27]. However, prior to the recent development of a satisfactory single-shot HCO PLIF technique [28], instantaneous visualization of the HCO radical in turbulent flames was rare. As an alternative approach, the product of OH and CH_2O has been proposed as a qualitative heat release surrogate because it can be related to HCO

production through one of the major HCO formation reactions $CH_2O+OH \rightarrow H_2O+HCO$ [29, 30]. Although this method has only been experimentally verified in laminar flames, it has been employed widely in many experimental studies of turbulent flames [31-36] owing to the experimental feasibility. To the best of the authors' knowledge, the correlation between HCO and the product of OH and CH_2O in turbulent flames, however, has not been experimentally investigated. The direct comparison of them in the present work presents a special interest to revisit the validity of different heat release surrogates in flames with various turbulence intensities.

Taking the advantage of multi-scalar imaging in the present work, correlations between different scalars were analyzed on both single-shot and statistical basis. The experimentally resolvable small-scale structures in flames resided in both the TRZ and DRZ regime are identified through the instantaneous correlated structures between scalars. Statistical analysis were performed to investigate the correlations of various scalars with temperature in flames.

2. Experimental Setup

Figure 1(a) shows the experimental setup employed, which includes a Nd:YAG laser for CH_2O excitation and Rayleigh scattering thermometry at 355 nm, a dye laser for OH excitation at 283.55 nm, and an Alexandrite laser for excitation of CH and HCO at 387.3 nm and 259 nm, respectively. The shot-to-shot fluctuations of all laser energies were below 1%, and the 355-nm laser radiation was tuned to *s*-polarization by a half-wave plate to maximize the Rayleigh signal. Further details on the laser-diagnostic system and LIF excitation-detection schemes can be found in [23, 28]. Special attention has been paid in the present work to ensure interference-free detection of HCO [28] and CH [37] signals. The CH/HCO LIF emission spectra have been

recorded in both laminar and turbulent flame conditions, and no detectable spectral interference signal has been found. Laser beams were spatially combined and focused by a cylindrical lens (f=-40 mm) and a spherical lens (f=200 mm) into a laser sheet of ~20 mm height. By slightly adjusting the laser beam divergences using telescope systems, tightly focused laser sheets were obtained at the top of the jet center for all beams. The thickness of the combined laser sheet was measured to be less than 100 μm.

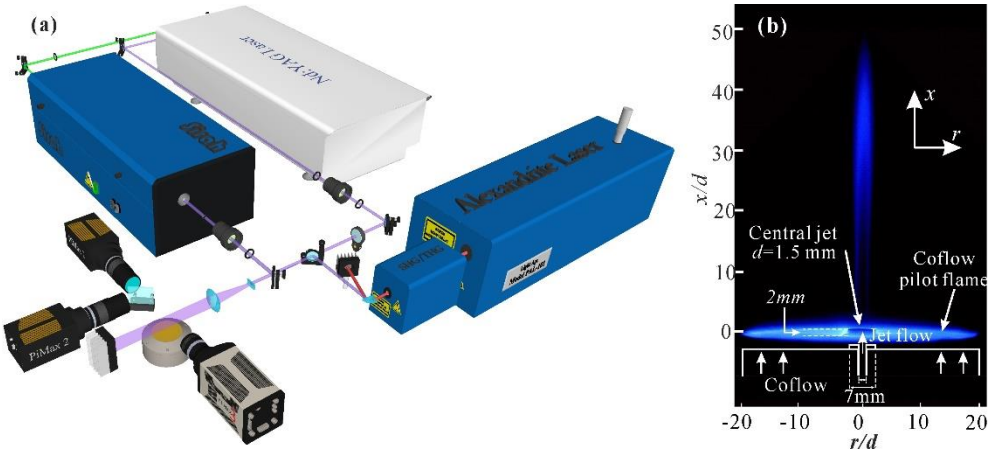

Figure 1. (a) Experimental setup for simultaneous multi-scalar imaging measurements, and (b) photograph of a LUPJ flame with a schematic plot of the burner employed.

The detection system included three Intensified CCD (ICCD) cameras. Two orthogonally-oriented cameras were arranged for detection of OH and CH_2O (or Rayleigh) signals which were separated using a beam splitter (R>99.9% @ 260-330 nm and T>95% @ 350-600 nm). Performance of the beam splitter was upgraded compared with the one employed previously [23] to enable simultaneous T/CH/OH measurements. The CH (or HCO) signal was detected by the third camera. The camera gates for all scalars were set to less than 50 ns and proper optical filters (see [23] for details) were employed for each scalar for background rejection.

Background images for all scalars were measured with identical experimental configurations but lasers blocked, which show no additional signals (e.g. flame chemiluminescence) being detectable. All images of scalars were processed by background subtraction, flat-field correction, and pixel-by-pixel image correlation. By analyzing the smallest resolvable structures of a resolution target (USAF-1951) imaged with the same optical system, the CH/HCO camera showed a spatial resolution of 56 μm and the OH and CH_2O/T cameras showed a spatial resolution of 74 μm. The signal-to-noise ratios (SNRs) of the measured scalars were estimated to be better than 17 for CH, 8 for HCO, 32 for OH, 28 for CH_2O in stoichiometric flames studied, and 24 for Rayleigh signals measured from cold air. To further suppress noise, median filters with filter sizes of 4×4 pixels for species scalars and of 8×8 pixels for temperature were applied. Given the SNRs achieved and species concentrations estimated from CHEMKIN simulation under relevant condition [24], the detection limits were estimated to be ~ 100 ppm for OH, 40 ppm for CH_2O, 3 ppm for HCO and 0.1 ppm for CH at 1000 K.

The simultaneous multi-scalar imaging measurements were performed on a hybrid jet burner, Fig.1 (b), known as the LUPJ (Lund University Pilot Jet) burner which consists of a center jet (1.5 mm in diameter) surrounded by a 61-mm diameter porous plug. A premixed methane/air mixture with an equivalence ratio Φ=0.9 was supplied at an inlet flow speed of 0.3 m/s to the porous plug so that a laminar flat flame was stabilized and acted as a pilot flame to support the central high-speed turbulent jet flames. The studied jet flame conditions are listed in Table 1 with each condition labeled as LUPJα-β where α represents the equivalence ratio and β represents the bulk flow velocity (U_0) at the jet exit. A laminar jet flame (LUPJ10-11) was run to provide a reference to the turbulent flames studied. The laminar flame velocity (S_L) was

determined experimentally from the relation $S_L=U_0\times\sin\theta$ where θ is the half angle of the flame cone determined from the flame height (indicated by OH image) and jet nozzle radius. The thermal laminar flame thickness (δ_L) was determined from the measured temperature field as $\delta_L=\frac{T_p-T_u}{|\nabla T|_{max}}$ where T_p and T_u are the temperature of the products and the unburned reactants, respectively. For comparison, S_L and δ_L were also determined from numerical simulation of an ideal planar free-propagation flame using the GRI 3.0 chemical kinetic mechanism [38]. As shown in Table 1, the values of S_L and δ_L determined from experiments are higher than those from the numerical simulations by about 10% because the pilot flame has a direct heating effect on the jet flames, which becomes more significant in leaner cases [24]. Following our the previous study [24], to consistently account for the effects of the pilot flame and the burner configuration in evaluating turbulent statistical quantities, the experimental S_L and δ_L were adopted in the present work. For turbulent flames, U_0 was varied from 66 m/s up to 418 m/s to cover a wide operational range from the TRZ regime to the DRZ regime. Based on the flow-field measurements reported earlier [24], the integral scale (l_0) and the turbulent intensity (u'/S_L) was estimated at 30 jet diameters (x/d=30), which is at the middle of the axial range where turbulence intensities peak. The turbulent Reynolds number (Re_t), the Kolmogorov scale (η) and the Karlovitz number (Ka) of each turbulent flame were calculated accordingly based on the formulations given by Peters [4] as listed in the footnote of Table 1. The Kolmogorov scales for the investigated flames are slightly finer but comparable to the spatial resolution that the multi-scalar imaging system provided. Following Peters [4], the LUPJ10-66 and LUPJ10-110 flames are located in the TRZ regime, while the LUPJ10-165 flame falls on the border of the DRZ regime, and the rest of flames are in the DRZ regime.

Table 1. Summary of investigated laminar and turbulent flames.

Laminar flame								
Flame Code	Φ	U_0 (*m/s*)	$S_{L,Exp}$ (cm/s)	$S_{L,CHEM}$ (cm/s)	$\delta_{L,Exp}$ (mm)	$\delta_{L,CHEM}$ (mm)		
LUPJ10-11	1.0	11	42.5	37.5	0.48	0.44		
Turbulent flames								
Flame Code	Φ	U_0 (*m/s*)	Re_{jet} [a]	Re_t [b]	l_0 (*mm*)	η [c] (μm)	u'/S_L	l_0/δ_L	Ka [d]
LUPJ10-66	1.0	66	6306	95	2.9	96	16	6.0	25
LUPJ10-110		110	10510	190		57	31		70
LUPJ10-165		165	15764	238		49	39		98
LUPJ10-220		220	21019	317		39	52		151
LUPJ10-330		330	31539	476		29	78		277
LUPJ10-418		418	39949	603		24	99		395

[a.] Jet Reynolds number, $Re_{jet}=(U_0\times d)/\nu$, ν is the kinematic viscosity @ 298 K; [b.] Turbulent Reynolds number, $Re_t=(u'\times l_0)/(S_L\times\delta_L)$; [c.] Kolmogorov length scale, $\eta=l_0\times Re_t^{-3/4}$; [d.] Karlovitz number: $Ka=\{(u'/S_L)^3\times(\delta_L/\ l_0)\}^{1/2}$

3. Marker of flame structures

The structure of laminar premixed methane/air flame can be characterized using a three-zone asymptotic model [39-41]: (a) a preheat zone where the temperature is lower than the cross-over temperature and chemical reactions are at inert; (b) an inner-layer where the fuel is consumed and combustion intermediate CO and H_2 are formed; and (c) an oxidation layer where CO and H_2 are oxidized to form CO_2 and H_2O. Among the reactions involved in the inner layer and given the species available in the multi-species PLIF measurements of the present study, the inner layer can be characterized by measuring the reaction rates of the following reactions,

$HCO+OH\rightarrow CO+H_2O$ (I)

$CH+OH\rightarrow HCO+H$ (II)

$CH_2O+OH\rightarrow H_2O+HCO$ (III)

Reactions (I) and (II) characterize one of the HCO/CH consumption paths in the inner layer, and Reaction (III) is one of the major reactions responsible for HCO formation. The forward reaction rates of Reactions (I) to (III) are expressed as $R_{HCO,c}=k_I[HCO]\times[OH]$, $R_{CH,c}=k_{II}[CH]\times[OH]$ and $R_{HCO,f}=k_{III}[CH_2O]\times[OH]$, respectively, where the brackets indicate species concentrations, k the reaction rate constant and the subscripts f and c denote the formation or consumption reactions of the species associated. According to the mechanism of Glarborg [42], the k_I and k_{II} are temperature independent, while $k_{III}(T)= 7.8\times10^7T^{1.6}exp(531/T)$. Therefore, the corresponding reaction rates can be experimentally measured as $R^*_{HCO,c}=[HCO]_{LIF}\times[OH]_{LIF}$, $R^*_{CH,c}=[CH]_{LIF}\times[OH]_{LIF}$ and $R^*_{HCO,f}= k_{III}(T)[CH_2O]_{LIF}\times[OH]_{LIF}$, where the subscript LIF on the right-hand side of the equations is introduced to distinguish it from the concentration expression, and the superscript * on the left-hand side of the equations indicates that these rates are based on the PLIF signal intensity, rather than the actual concentrations of these species. Here, it is assumed that LIF signals are proportional to their concentrations, which could hold true as it is shown in our previous study [24] that corrections of LIF signals for quantification have a minor impact on the measured species profiles in the laminar flame LUPJ10-11. Furthermore, in many previous experimental studies [31, 32] for measuring $R^*_{HCO,f}$, $k(T)$ was usually neglected as simultaneous temperature measurements were not always available and the temperature range over which the reaction occurs may be argued to be narrow. Therefore, qualitative experimental measurement of HRR region is further simplified as the direct product of OH and CH_2O PLIF intensities, $[OH]_{LIF}\times[CH_2O]_{LIF}$. This experimental method could be justified if the aim is to identify regions where HRR is noticeable.

In addition to the reaction rate imaging described above, it is noted that CH and HCO

radicals are formed and consumed in the inner layer, both being good markers of the inner layer of the reaction zone. To access the lifetimes of the CH and HCO radicals under various conditions, numerical simulations were performed using a closed homogeneous reactor model in the CHEMKIN software with the mechanism of Glarborg [42]. The reactor temperature was varied from 800 K to 2000 K, to cover the reaction zone temperatures in flames. Two mixtures compositions have been examined; a stoichiometric methane/air mixture (i.e. 8.6% CH_4, 72.2% N_2 and 19.2% O_2) and a mixture made up of the combustion products of the pilot flame (i.e. 9.45% CO_2 and H_2O, 2.1% O_2 and 79% N_2). The initial mole fractions of CH and HCO in the mixtures were set to 4 and 40 ppm, respectively, which correspond approximately to their peak mole fractions in an adiabatic stoichiometric methane/air flame. The CH and HCO concentrations follow exponential decays, and their lifetimes are defined as the time at which the concentration becomes $1/e$ of the initial values. For the lifetime estimation in the simulations, HCO/CH consumption mechanisms are dominant, and HCO and CH formation (e.g. in the stoichiometric methane/air mixture) due to auto-ignition will not influence the estimation of HCO and CH lifetimes as consumption of the initial CH and HCO radicals will end much earlier before the CH/HCO formation due to the long induction time of the auto-ignition process. Thus, in both cases involvements of reactions with H, O, and OH radicals are negligible. As can be seen in Fig. 2(a-b), both CH and HCO radicals have lifetimes ranging from tens nanoseconds to hundreds of nanoseconds, and the major reactions responsible for HCO/CH consumption under the simulated conditions are also shown.

It is estimated that a short time scale on sub-microseconds level does not allow the diffusion of HCO/CH radicals to the preheat zone without being consumed. Even for turbulent

flames, where the transport of reactive species is by virtue of eddy transport, the penetration length of CH and HCO is still very short. The maximal turbulent velocity of the LUPJ flames studied is approximately 42 m/s [24], giving a distance of typically a few micrometers that the CH or HCO radicals may be transported. It is worthy to point out that both CH and HCO can be depleted rapidly by O_2 through nearly temperature independent reactions (see reactions listed in Fig.2), which are two of the major CH/HCO consumption reactions. In the flames investigated in the present work, O_2 is abundant and widely exists in space as the jet flames and the pilot flame were operated at stoichiometry and Φ=0.9, respectively, and oxygen could also be entrained from ambient air for cases of high U_0 (e.g. LUPJ10-330 and LUPJ10-418). Therefore, it can be concluded that CH and HCO radicals that exist in space are typically formed through reactions that occur locally, being good markers for distributed reactions.

Together with the HCO/CH fields and the reaction rate imaging of the $R^*_{HCO,f}$ (or $[OH]_{LIF}\times[CH_2O]_{LIF}$), $R^*_{HCO,c}$ and $R^*_{CH,c}$ fields, the OH gradient $|\nabla[OH]|_{2D}$ as well as the temperature gradient $|\nabla T|_{2D}$ are computed additionally from the scalar fields obtained to characterize the structures of laminar flames (section 4) and turbulent flames (section 5).

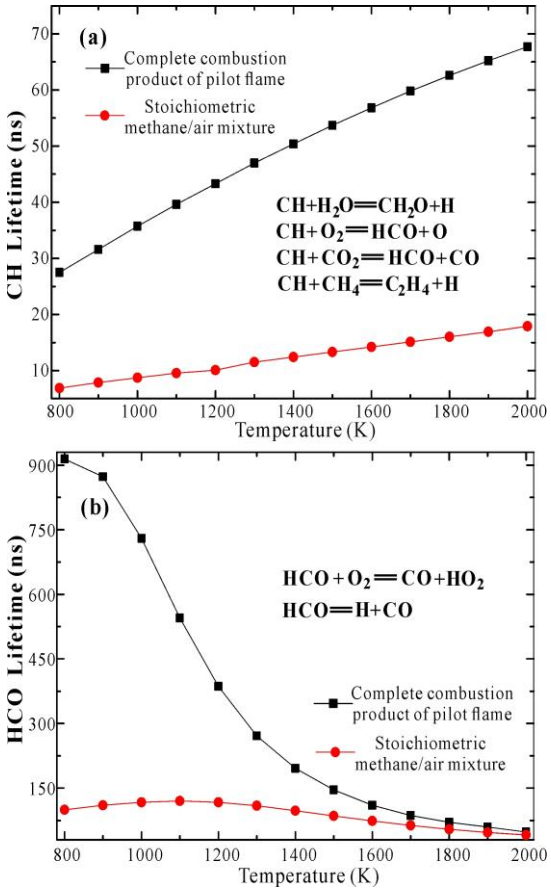

Figure 2. Numerical simulations of (a) CH and (b) HCO lifetimes at various temperatures in a closed homogeneous reactor with a mixture composition corresponding to that of combustion product of the pilot flame (squares), and alternatively a stoichiometric methane/air mixture (circles). A number of major reactions responsible for CH/HCO consumption under the simulated conditions are shown.

4. Structure of laminar flames

Figure 3 shows the structure of the laminar flame LUPJ10-11 characterized using various scalars. Each image is an average of 100 single-shot images. It is noted that the scalar fields after ensemble averaging are not smeared out comparing with the single-shot images, which indicating an excellent stability of the laminar flame under the current flow condition. It is seen that CH and HCO as the inner layer reaction zone markers have nearly identical structure with similar thickness. The high OH gradient, $|\nabla[OH]|_{2D}$, are also shown in a very thin region, slightly

downstream the HCO/CH layer. Located slightly upstream of the CH and HCO layers is the preheat zone marked by CH_2O, which also appears thin in major part of the flame, except that around the flame tip where the preheat zone merges due to the flame topology. The CH_2O field coincides well the low temperature zone when comparing with the temperature field. The temperature gradient, $|\nabla T|_{2D}$, has a peak value of approximately 3000 K/mm and spatially correlates more closely with the downstream of the CH_2O layer, except in the flame tip region where the reaction zone is slightly broader due to the high curvature at the flame tip.

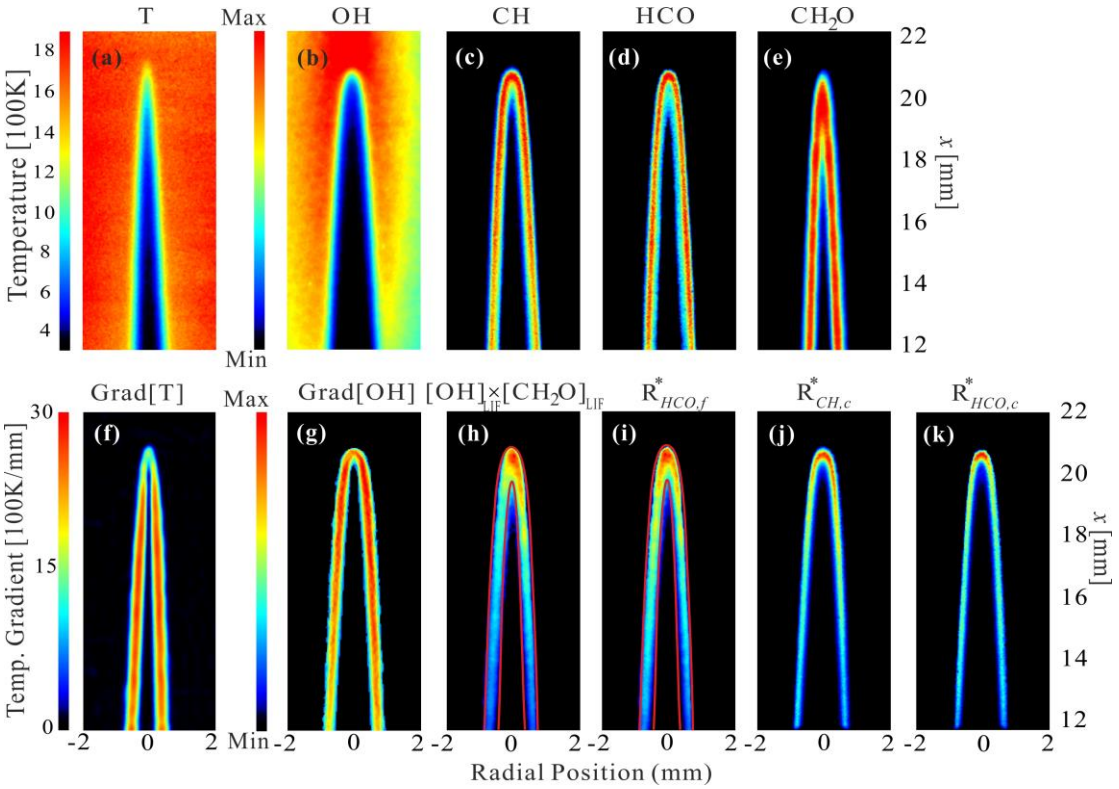

Figure 3. Example of (quasi-simultaneous) imaging of (a) temperature and species of (b) OH, (c) CH, (d) HCO, (e) CH_2O, (f) temperature gradient ($|\nabla T|_{2D}$), (g) OH gradient ($|\nabla[OH]|_{2D}$), (h) product of OH and CH_2O ($[OH]_{LIF}\times[CH_2O]_{LIF}$) and the relative reaction rates of (i) $R^*_{HCO,f}$, (j) $R^*_{CH,c}$ and (k) $R^*_{HCO,c}$ for LUPJ10-11.

Figure 3h-3k give further insights into the laminar flame structure. As pointed out by Najm et al. [17], HCO concentration is a good marker of peak HRR and can be also related to $R^*_{HCO,f}$, i.e. the rate of the reaction III. In Fig. 3h and 3i isosurface of 10% maximal intensity of HCO

(red curve) is superimposed in the fields of $R^*_{HCO,f}$ and $[OH]_{LIF}\times[CH_2O]_{LIF}$ for comparison. It can be seen that the $R^*_{HCO,f}$ and $[OH]_{LIF}\times[CH_2O]_{LIF}$ remain similar, suggesting that the inclusion of temperature dependence in the $k_{III}(T)$ calculation has minor impact on $R^*_{HCO,f}$ due to the small temperature range associated with the reaction. In general both $R^*_{HCO,f}$ and $[OH]_{LIF}\times[CH_2O]_{LIF}$ field overlaps well with HCO in space, indicating a good spatial correlation between them as suggested by the experimental and numerical results shown by Najm et al. [29]. In the following discussion of turbulent flames, $[OH]_{LIF}\times[CH_2O]_{LIF}$ is used as one of the markers for the HRR or HCO formation region when instantaneous temperature data is not available. It can be seen from Fig. 3j - 3k that $R^*_{HCO,c}$ and $R^*_{CH,c}$ are similar and appear even thinner than the CH and HCO layers. At the flame tip, the fields of $R^*_{HCO,f}$, $R^*_{HCO,c}$ and $R^*_{CH,c}$ all show higher values than in the other part of the flame, which indicates a strong stretch effect at the flame tip.

The discussion above demonstrated that the reaction zone in a laminar flame can be properly characterized using several scalars such as HCO, CH, OH and gradients of OH as well as the reaction rate imaging of $R^*_{HCO,f}$(or $[OH]_{LIF}\times[CH]_{LIF}$), $R^*_{HCO,c}$ and $R^*_{CH,c}$ within the experimental resolution of the present work. In the following we apply the analysis to study of the structures of turbulent premixed flames.

5. Turbulent flames in the TRZ and DRZ regimes

5.1 Structures of turbulent flames in the TRZ and DRZ regimes

From the HCO/CH_2O/OH dataset, examples of instantaneous turbulent flame structures for two flames (i.e. LUPJ10-110 and LUPJ10-418) are shown in Fig.4. First of all, as discussed in our previous studies [23, 24], a strong anti-correlation between OH and CH_2O intensities can be

found in both flames. This is due to the fuel oxidization chemistry that the reaction rate of the Reaction III is so rapid that it prohibits CH_2O from coexisting with the OH radicals to an appreciable amount regardless of the combustion mode. For the LUPJ10-110 flame shown in Fig. 4A, the preheat zone as marked by CH_2O is significantly broadened while the reaction zone is overall thin. Similar to the laminar flame discussed earlier, the reaction zone of the LUPJ10-110 is well represented by both HCO, $[OH]_{LIF}\times[CH_2O]_{LIF}$, $R^*_{HCO,c}$ and $|\nabla[OH]|_{2D}$ from which close agreement in regard to their spatial distribution can be found. It appears that the layers of HCO, $[OH]_{LIF}\times[CH]_{LIF}$ and $|\nabla[OH]|_{2D}$ are generally similar in thickness, while $R^*_{HCO,c}$ is even slightly thinner compared with the HCO thickness. In addition, $|\nabla[OH]|_{2D}$ appears to be slightly smeared in some regions with sharp cusps in the reaction zone, and a weaker OH gradient can also be observed in the post-flame region as OH concentration decreases to its equilibrium state from the super-equilibrium state in the reaction zone. The result support Peters' TRZ regime theory: in the TRZ regime, the preheat zone (CH_2O layer) is broadened while the inner layer (indicated by HCO, CH, $[OH]_{LIF}\times[CH_2O]_{LIF}$, $R^*_{HCO,c}$ and $R^*_{CH,c}$) remains essentially as thin as that in the laminar flames. It should be pointed out, however, that the thin inner layer is highly wrinkled, and intensities of these scalars vary greatly, owing to the variation of flame stretch along the flame front.

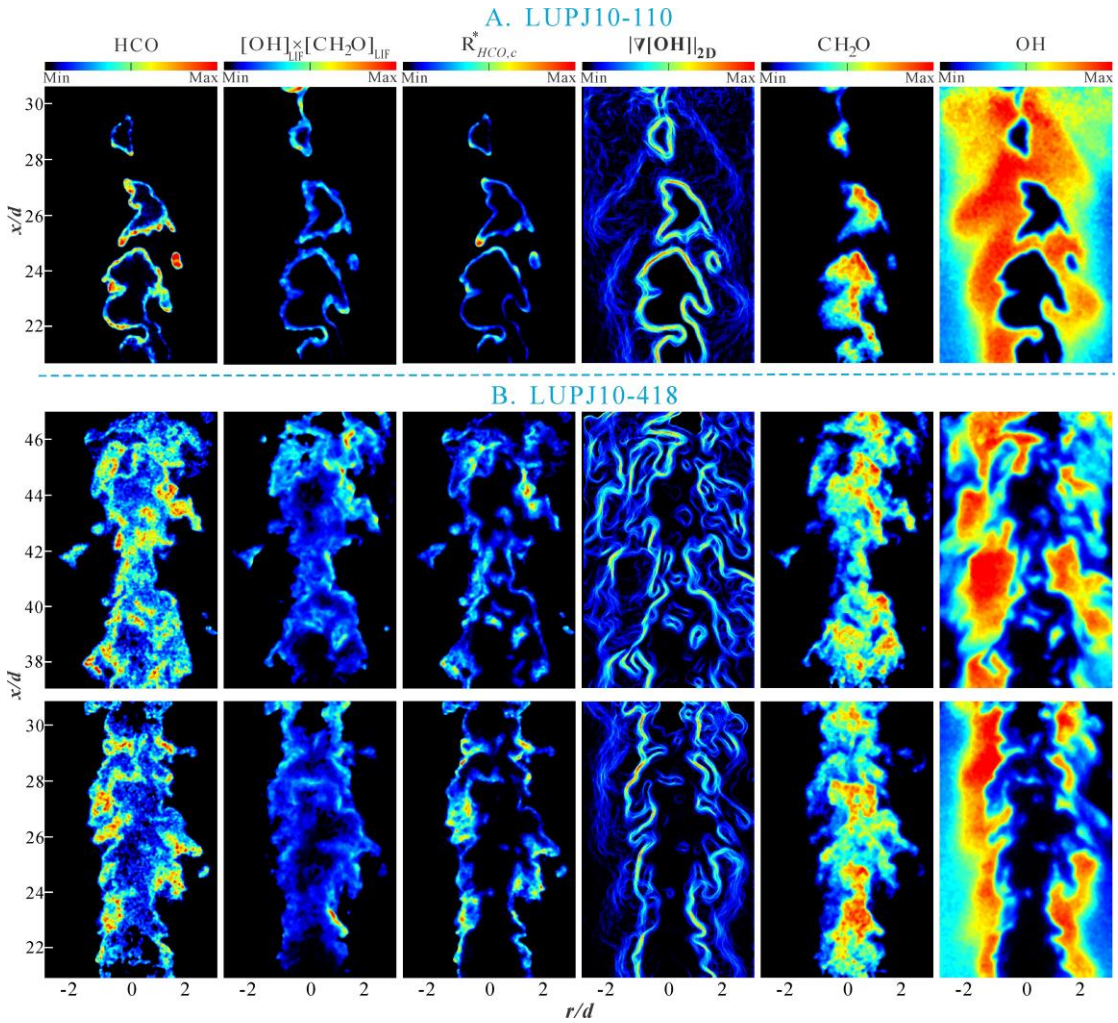

Figure 4. Examples from the HCO/CH_2O/OH dataset: simultaneous snapshots of reactive scalars (i.e. HCO, CH_2O and OH), product of OH and CH_2O ($[OH]_{LIF}\times[CH_2O]_{LIF}$), OH gradient ($|\nabla[OH]|_{2D}$) as well as the relative reaction rate $R^*_{HCO,c}$ for flames LUPJ10-110 and LUPJ10-418.

In contrast to the flamelet-like structure discussed above, Fig. 4B shows an essentially different structure of the flame LUPJ10-418. HCO radicals are broadened/distributed in space, providing a direct evidence of distributed reactions as discussed earlier. Accompanied with the HCO broadening, the CH_2O/OH overlapping region (HRR region) becomes thicker as indicated by the broadened distribution of $[OH]_{LIF}\times[CH_2O]_{LIF}$, being an additional evidence of distributed reactions which has also been recently confirmed by experimental studies of similar flames from Driscoll's group [43, 44]. It is also of interest to note that the $R^*_{HCO,c}$ field is likewise broadened in certain regions but overall to a less extent. In fact, the dark regions of $R^*_{HCO,c}$

where HCO is distributed corresponds to smaller values of $R^*_{HCO,c}$, being less than 1/10 of its maximum value in the same image. The $|\nabla[OH]|_{2D}$ field appears highly convoluted. Yet despite the OH gradients stemming from the post-flame region, regions with relatively high OH gradients can still be visible in thin layers. On the other hand, relatively low OH gradients with fine filament-like structures appear on the $|\nabla[OH]|_{2D}$ field in some regions where CH_2O/HCO signals prevail. This is a unique feature of the flame structure in the DRZ regime that is significantly different from that in the flamelet regime.

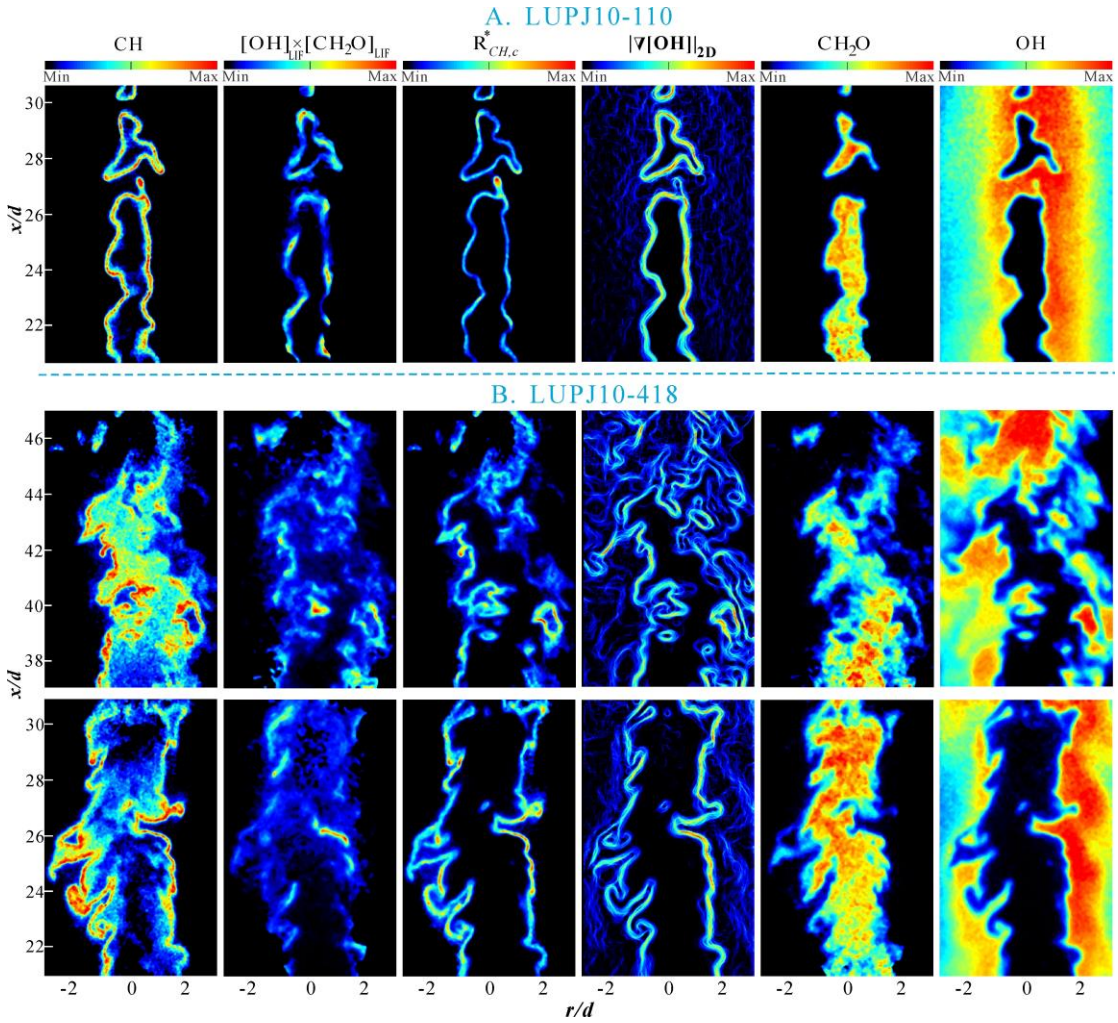

Figure 5. Examples from the CH/CH_2O/OH dataset: simultaneous snapshots of reactive scalars (i.e. CH, CH_2O and OH), product of OH and CH_2O ($[OH]_{LIF}\times[CH_2O]_{LIF}$), OH gradient ($|\nabla[OH]|_{2D}$) as well as the relative reaction rate $R^*_{CH,c}$ for flames LUPJ10-110 and LUPJ10-418.

The observations discussed above can be associated with the fact that an appreciable amount of OH radicals (and likely other radicals such as H and O radicals) has been transported away from the reaction zone to regions of reactants, which is considered to be one of the major reasons for the occurrence of distributed reactions in this type of flames [24]. Very similar experimental observations have also been made from the CH/CH_2O/OH dataset as shown in Fig.5 taken at a different instance of time than that in Fig. 4.

It is noteworthy that the $[OH]_{LIF}\times[CH_2O]_{LIF}$ fields shown in both Fig.4 and Fig.5 are more blurred and detailed flame structures are less resolved compared with other scalars. This is because OH and CH_2O distributions are in general anti-correlated and overlap at regions of relatively low signals, making the pixel-by-pixel calculation of $[OH]_{LIF}\times[CH_2O]_{LIF}$ susceptible to, e.g., experimental detection limits, SNRs and non-ideal background subtraction. In the present work, to minimize the uncertainty, the image backgrounds were recorded and subtracted with special care. The experimental detection limits and SNRs of OH and CH_2O (as given in the experimental setup section) are sufficient for the reaction zone identification but could be insufficient in resolving detailed flame structures. Although these concerns are technical details, it is nontrivial if $[OH]_{LIF}\times[CH_2O]_{LIF}$ is used to determine discontinuation or broadening of the reaction zone that could have significant implications to the understanding of turbulence-flame interaction. For example, significant broadening of the $[OH]_{LIF}\times[CH_2O]_{LIF}$ in the burned/unburned regions can be an artifact of improper background subtraction. Erroneous conclusions could be drawn if attention was not paid to these technical issues.

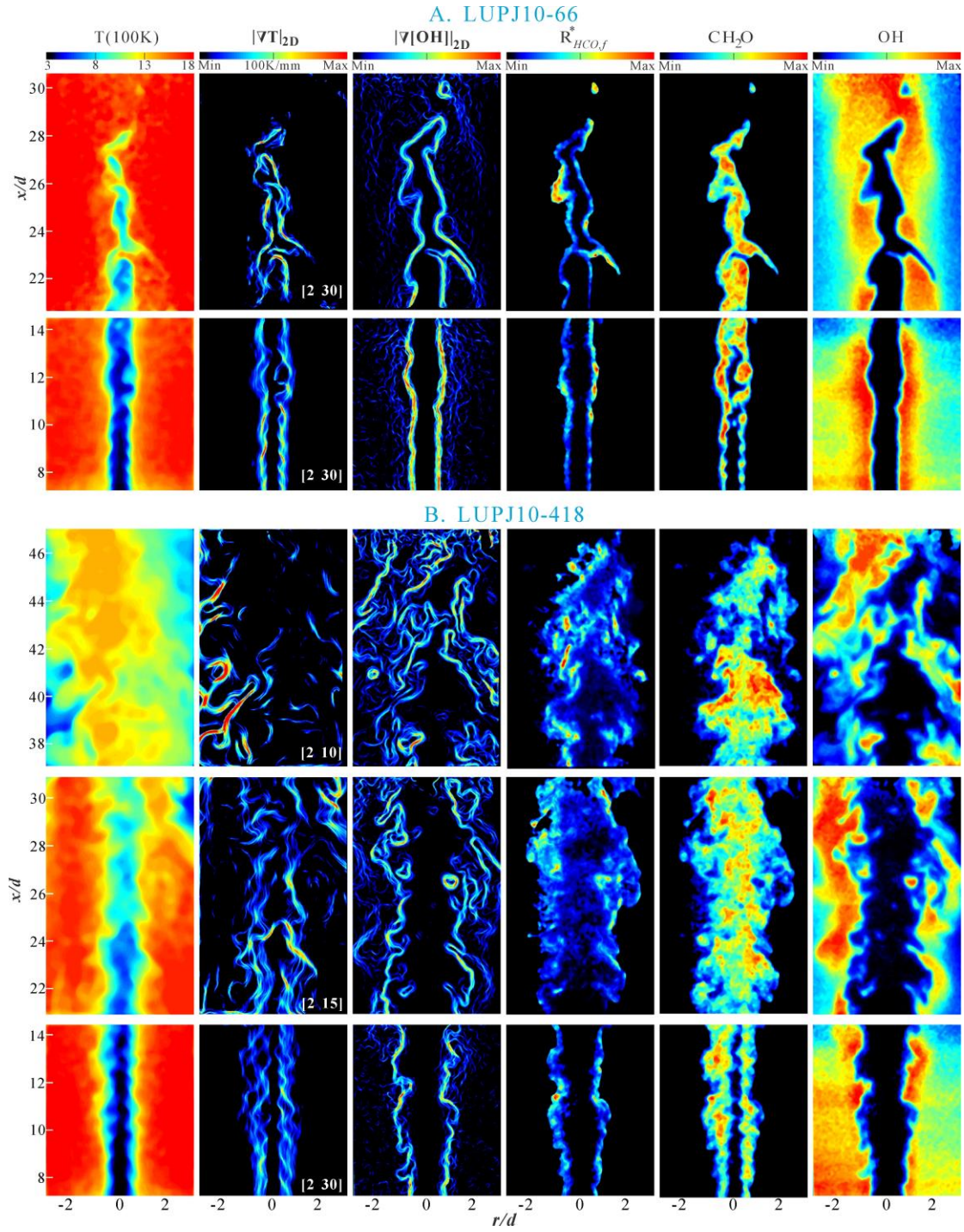

Figure 6. Examples from the T/CH_2O/OH dataset: simultaneous snapshots of scalars (i.e. T, CH_2O and OH), OH gradient ($|\nabla[OH]|_{2D}$), temperature gradient ($|\nabla T|_{2D}$) as well as the relative reaction rate $R^*_{HCO,f}$ from the flames LUPJ10-110 and LUPJ10-418.

In addition to the instantaneous structures of the reactive scalars shown above, temperature fields and temperature gradient ($|\nabla T|_{2D}$) fields from T/CH_2O/OH dataset are shown in Fig.6 for

flames LUPJ10-66 and LUPJ10-418. The absolute range of the $|\nabla T|_{2D}$ displayed in the color map is indicated in the lower right corner of each $|\nabla T|_{2D}$ image with the unit of 100 K/mm. For flame LUPJ10-66 that is in the TRZ regime, a significant turbulence distortion in the temperature field can already be observed: temperature iso-surfaces are no longer parallel and the temperature in the unburnt region increases gradually along the axial direction. In the $|\nabla T|_{2D}$ field, it is shown that higher temperature gradients are seen at slightly upstream of the reaction zone (marked by $R^*_{HCO,f}$) and primarily overlap with the preheat zone (marked by CH_2O). Similarities between the $|\nabla T|_{2D}$ and the reaction zone in terms of wrinkling can be identified. Although the magnitude of the temperature gradients in flame LUPJ10-66 is in general lower than that in the laminar flame (cf. Fig.3), high temperature gradients that are comparable to that under the laminar flamelet condition can still be identified in certain localized regions. For the LUPJ10-418 flame, the $|\nabla T|_{2D}$ field is rather complex in which fine filament-like structures prevail, sharing less similarities with the distributed CH/HCO layers. The absolute values of the $|\nabla T|_{2D}$ decrease significantly along the axial direction.

5.2 HCO-$[OH]_{LIF}\times[CH_2O]_{LIF}$ Correlation

It can be seen from Fig.4 that the intensity variation in the $[OH]_{LIF}\times[CH_2O]_{LIF}$ field is hardly reflected in the HCO field, neither it is in the laminar flame (cf. Fig. 3). Instead, to examine the correlation between HCO and $[OH]_{LIF}\times[CH_2O]_{LIF}$, the instantaneous thicknesses of the HCO and $[OH]_{LIF}\times[CH_2O]_{LIF}$ layer were compared, where the thickness was defined as the full radial width (at minimal detectable intensity) divided by two which accounts for the contribution from the two flame brushes of the present cone shaped flame. As an example, the thickness of the

instantaneous HCO and $[OH]_{LIF}\times[CH_2O]_{LIF}$ layers evaluated at x/d=24 over more than 300 samples is shown in Fig.7 (a1) and (b1) for flames LUPJ10-66 and LUPJ10-418, respectively. The variation of instantaneous thickness is potentially due to flame thinning/thickening resulted from flame/turbulence interaction as well as topology of turbulent flames. The correlation is further presented as the scatter plots shown to the right of Fig.7. As can be seen, thickness of the HCO and $[OH]_{LIF}\times[CH_2O]_{LIF}$ layers in flame LUPJ10-66 is highly correlated from shot to shot while the correlation was reduced in flame LUPJ10-418. To quantify the correlation, the Pearson correlation coefficient ($R_{pearson}$) was introduced as:

$$R_{pearson} = \frac{\sum_i^N (x_i - X)(y_i - Y)}{\sqrt{\sum_i^N (x_i - X)^2}\sqrt{\sum_i^N (y_i - Y)^2}},$$

where N is total number of samples evaluated, and x_i and X (or y_i and Y) are the instantaneous and mean thicknesses of HCO (or $[OH]_{LIF}\times[CH_2O]_{LIF}$) layers. Values of ±1 for $R_{pearson}$ indicate complete positive/negative correlation, while a value of 0 indicates no correlation. The $R_{pearson}$ as well as the mean thickness of HCO and $[OH]_{LIF}\times[CH_2O]_{LIF}$ evaluated at x/d=24 are plotted against the turbulent Reynolds numbers for all turbulent LUPJ flames investigated and shown in Fig.8. It can be seen that the mean thicknesses of both HCO and $[OH]_{LIF}\times[CH_2O]_{LIF}$ consistently increase with increasing turbulent Reynolds number with the mean HCO thickness being slightly larger than that of the $[OH]_{LIF}\times[CH_2O]_{LIF}$. The mean HCO thickness at high turbulent Reynolds number is close to the integral scale (~ 2.9 mm) estimated from our previous flow-field measurements [24]. The $R_{pearson}$ coefficient decreases from 0.92 for flame LUPJ10-66 to 0.72 for flame LUPJ10-418, indicating a decorrelation between HCO and $[OH]_{LIF}\times[CH_2O]_{LIF}$ with increasing turbulence levels. Additionally, the mean thickness of HCO and $[OH]_{LIF}\times[CH_2O]_{LIF}$ as well as the $R_{pearson}$ correlation coefficient were also evaluated at

x/d=42 for flame LUPJ10-418 as shown by the empty symbols in Fig.8. It is shown in Fig.8 that the HCO mean thickness at *x*/d=42 remains similar to the one at *x*/d=24, while the $[OH]_{LIF}\times[CH_2O]_{LIF}$ mean thickness at *x*/d=42 decreases significantly. The corresponding $R_{pearson}$ coefficient is 0.43, indicating a further weakened correlation between HCO and $[OH]_{LIF}\times[CH_2O]_{LIF}$ under ambient air entrainment. This additional decorrelation is due to the entrainment of ambient air that can be occasionally observed for flames of high U_0 (i.e. LUPJ10-330 and LUPJ10-418) at higher axial locations (typically *x*/d>30) where OH could appear partially quenched while HCO, CH and CH_2O can still appear distributed widely in space [24]. In general, the trend of the decorrelation observed may be attributed to radicals such as H and OH that may have different distributions deviating from flamelet conditions under distributed reactions and/or ambient air entrainment. Therefore, contribution to HCO production from other important reactions with other radicals such as $H+CH_2O\rightarrow H_2+HCO$ can no longer be merely represented by the product of OH and CH_2O. It is interesting to note in Fig.8 that a sudden increase in the mean thickness of HCO and $[OH]_{LIF}\times[CH_2O]_{LIF}$ layers together with a sudden decrease of $R_{Pearson}$ were observed at Re_t from 190 to 238, correspondingly Ka from 70 to 98 (cf. Table 1). The sudden changes are a result of transition of flame mode from the TRZ regime to the DRZ regime. The associated critical Ka for this transition is close to the value of Ka=100 as suggested by Peters [4].

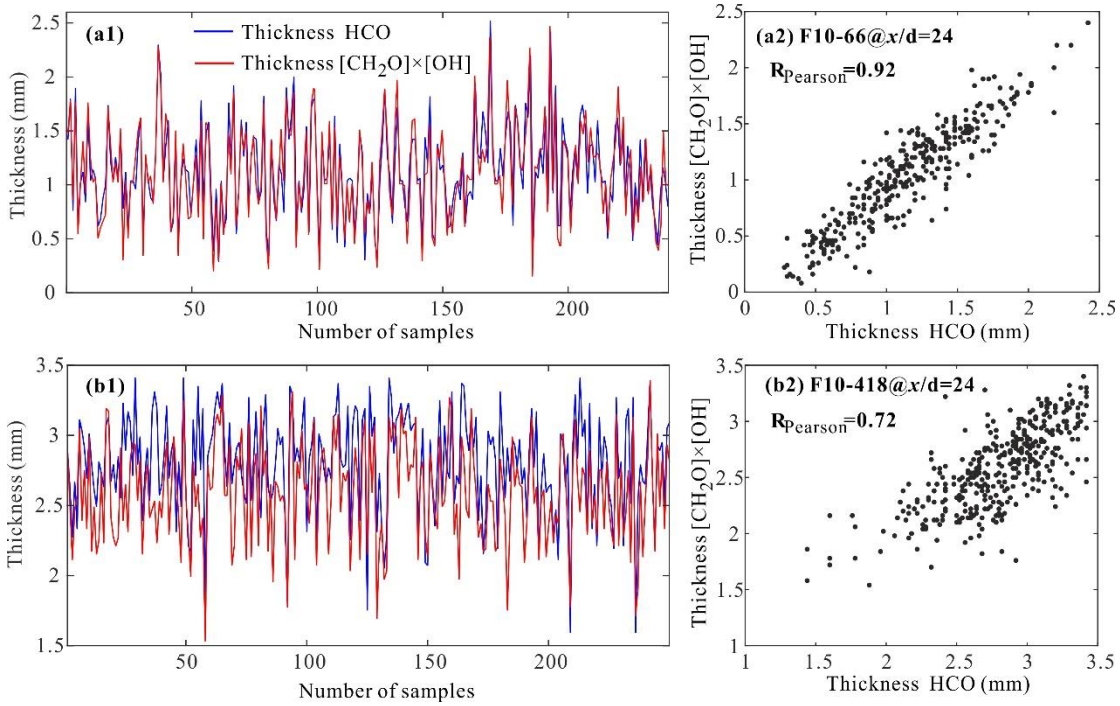

Figure 7. Examples of shot-to-shot variations in thickness of HCO (blue curve) and $[OH]_{LIF}\times[CH_2O]_{LIF}$ (red curve) layers evaluated at x/d=24 for flames (a) LUPJ10-66 and (b) LUPJ10-418. The correlation between HCO and $[OH]_{LIF}\times[CH_2O]_{LIF}$ thickness is shown to the right. A lower correlation between the HCO and $[OH]_{LIF}\times[CH_2O]_{LIF}$ is observed for the high Reynolds number LUPJ10-418 flame.

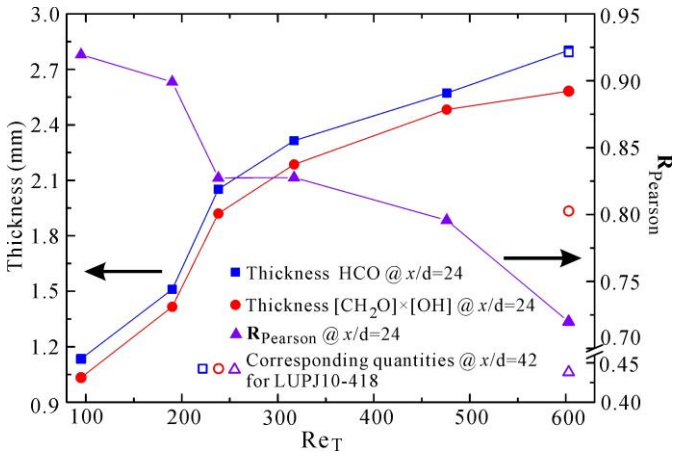

Figure 8. The mean thicknesses of HCO and $[OH]_{LIF}\times[CH_2O]_{LIF}$ layers (filled squares and circles) as well as the corresponding correlation coefficients ($R_{Pearson}$, filled triangles) evaluated at x/d=24 versus turbulent Reynolds numbers for all flames studied. The mean thicknesses and the correlation coefficient (empty symbols) evaluated at x/d=42 for the flame LUPJ10-418 are also presented for comparison.

5.3 Statistical analysis of turbulent flames in the TRZ and DRZ regimes

To quantify the effect of turbulence on the $|\nabla T|_{2D}$ field in flames, joint probability density functions (JPDFs) between $|\nabla T|_{2D}$ and temperature for flames LUPJ10-66, LUPJ10-220, and LUPJ10-418 at several axial locations (x/d=10, 24, 30 and 42) were calculated as shown in Fig.9. The $|\nabla T|_{2D}$ field was conditioned with the presence of CH_2O to properly select regions with reactions occurring and to exclude temperature gradients due to interactions with ambient air. The red dashed curve represents the corresponding laminar profile measured from flame LUPJ10-11, and the white dashed curve represents the mean temperature gradient. At x/d=10, the maximal temperature gradient for all flames investigated is generally lower than the corresponding laminar value, and with increasing jet speed (i.e. turbulence intensity), the maximal (mean) temperature gradient decreases and the temperature corresponding to the maximal temperature gradient shifts gradually from ~1000 K to ~800 K. This is consistent with the observation made by Dunn et al. [20] in jet premixed flames with a similar burner configuration. Moving downstream, the temperature range in which temperature gradients mostly prevail becomes gradually narrower, reaching about 800 K to 1500 K at x/d=42 for flame LUPJ10-418. The temperature gradient also decreases along the axial direction, and the temperature gradients at x/d=42 for flame LUPJ10-418 are typically less than 500 K/mm with the maximal mean temperature gradient around 150 K/mm, there being a characteristic property of the temperature field in distributed reactions.

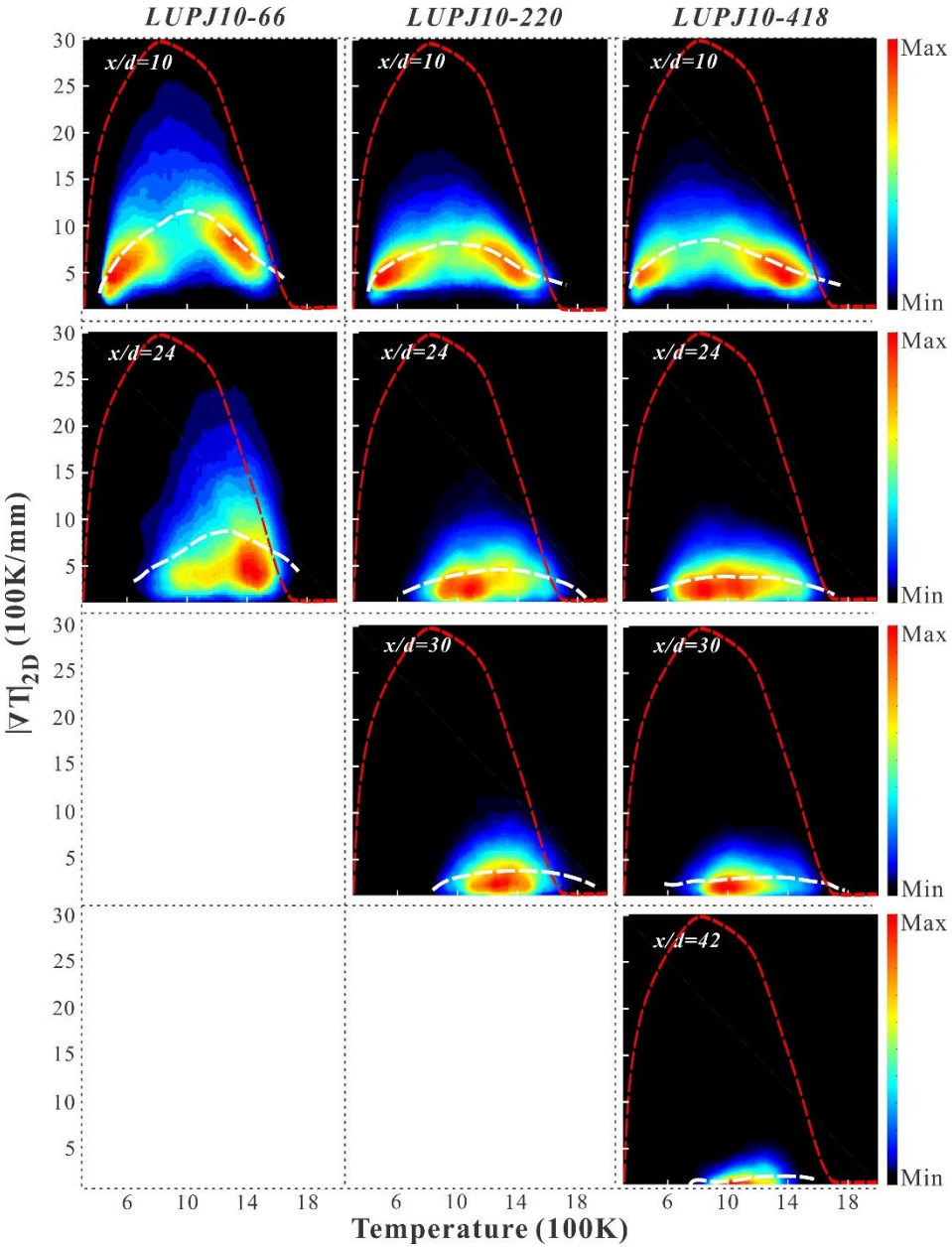

Figure 9. JPDFs of two-dimensional temperature gradient ($|\nabla T|_{2D}$) and temperature for the selected flames LUPJ10-66, LUPJ10-220 and LUPJ10-418 at axial locations of *x*/d=10, 24, 30 and 42. The red dashed curve represents the corresponding laminar profile measured from LUPJ10-11, and the white dashed lines represent the mean temperature gradient weighted by the probability.

Simultaneous CH and temperature measurements were performed by Mansour and Peters [45] to study a series of methane/air turbulent flames in the TRZ regime with a burner configuration similar to that of the present work. To compare with their results, similar analysis for the PDFs of the flame temperature conditioned at the maximal CH intensity was performed

for flames LUPJ10-66, LUPJ10-220 and LUPJ10-418 at *x*/d=10, 24 and 30 as shown in Fig.10. Although the flames investigated by Mansour and Peters were in the TRZ regime, the trends observed in both their PDF plots and Fig.10 are consistent. In general, for all flames studied, the probability distributions start approximately from 800 K (600 K in ref. [45]) and spread towards higher temperatures up to around 2000 K. The wide spread for peak CH signals in temperature was attributed to turbulence distortion of the preheat zone in the previous study [45]. The PDF profiles evaluated at higher axial locations tend to be more flat and peak at higher temperatures, a fact seems to be more pronounced for flame LUPJ10-66 in the TRZ regime.

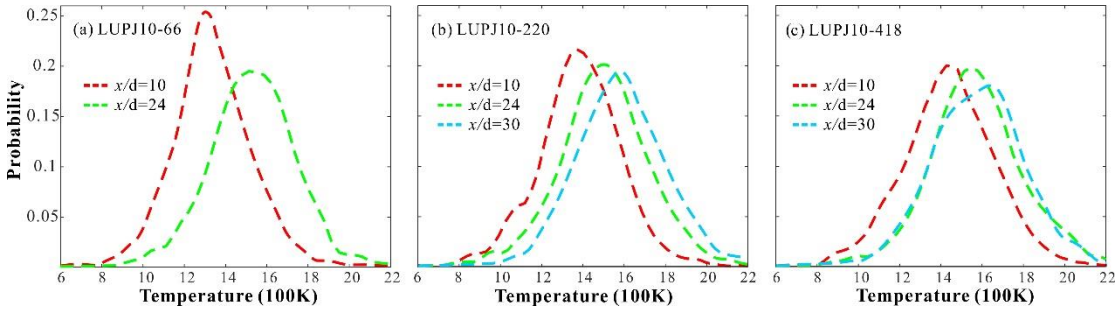

Figure 10. PDFs of the flame temperature conditioned at the maximal CH intensity evaluated for the selected flames, (a) LUPJ10-66, (b) LUPJ10-220 and (c) LUPJ10-418 at axial locations of *x*/d=10, 24 and 30.

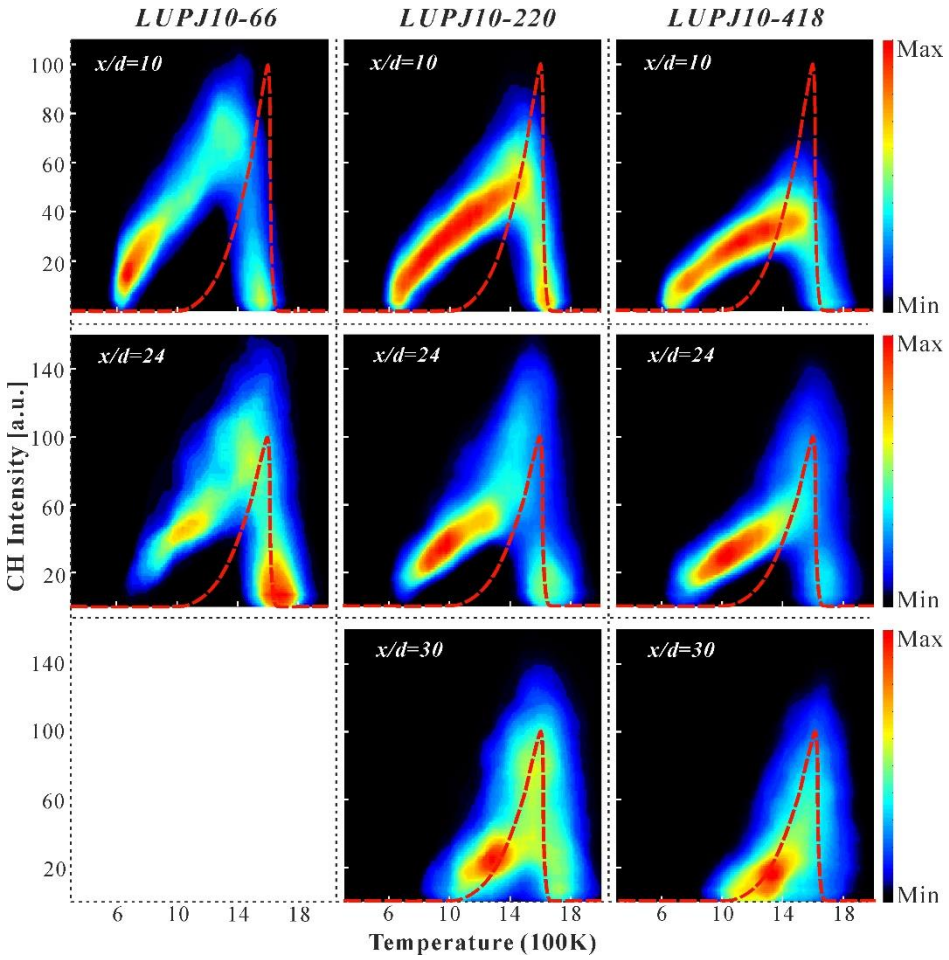

Figure 11. JPDFs of CH intensity and temperature for the selected flames, LUPJ10-66 (column 1), LUPJ10-220 (column 2) and LUPJ10-418 (column 3) at axial locations of *x*/d=10, 24 and 30. The red dashed curve represents the CH-T correlation measured in the laminar flame LUPJ10-11 for comparison.

In addition to the PDFs, the high SNRs of CH and T achieved in the present work allow for the calculation of JPDF of temperature and CH intensity as shown in Fig.11. The red dashed curve represents the CH-T profile measured in the laminar flame LUPJ10-11 for comparison. At *x*/d=10, the maximal CH intensity in flame LUPJ10-66 is comparable to the value of the laminar flame, while gradual reduction of CH signal intensity by up to 40% can be observed with increasing flow speed in the flame LUPJ10-418. Similarly, reduction of OH signals at *x*/d=10 by ~35% from the flame LUPJ10-66 to LUPJ10-418 was reported previously [24]. At locations further downstream, e.g., at *x*/d≥24, the maximal CH intensities for flames LUPJ10-

220/418 are comparable to that of LUPJ10-66 and higher than the peak value of the laminar flame. There are different reasons that can give rise to the spatial variation of CH/OH intensities along the flame height: (1) the high flame stretch rates near the burner exit that can delay the transition from the state of mixing of unburned fuel/air mixture with the hot gas from the pilot flame to the fully ignited stable flame state, and (2) the loss of heat and radicals from the flame to the burner surface. With increasing jet velocity, the latter will become less important while the former becomes more important; thus, it is likely that the main reason responsible for the lower CH and OH intensities in the near burner region (e.g. x/d=10) is the high flame stretch rates in the proximity of the burner exit.

It is interesting to note that the JPDF CH-T profiles in all flames, including the flame LUPJ10-66 in the TRZ regime, deviate significantly from the laminar profile, in particular in the low temperature region. The JPDF CH-T profiles of turbulent flames consist typically of two branches: (1) a rising branch of CH intensity in the low temperature region, in which the CH signals increase nearly linearly with temperature from ~ 600 K up to 1300 K for LUPJ10-66 and ~ 1500 K for LUPJ10-418 and (2) a decreasing branch of CH intensity within a narrow temperature range of approximately 1500 K to 1800 K. However, as seen from the laminar profile, CH signals are not expected to exist at temperatures as low as ~ 600 K. It is also noteworthy that the dual-branch behavior is also observed in the JPDF CH_2O-T profile at locations upstream (e.g. x/d=10) as reported in our previous study [24]. Nevertheless, a few important differences can be noticed. The JPDF CH_2O-T profile starts at ~ 300 K to 400 K and peaks at around ~ 700 to 900 K which is about 600 K lower than the temperatures that the JPDF CH-T profiles peak. The peak of the JPDF CH_2O-T profile shifts toward lower temperatures

with increasing U_0, which is in contrast to the trend observed for the JPDF CH-T profiles. In addition, the rising branch for the JPDF CH_2O-T profiles completely disappears at x/d≥24, leaving a decreasing branch with a long tail spreading over a wide temperature range. In contrast, the rising branch of the JPDF CH-T profile clearly persists at x/d=24, and the decreasing branch is much sharper than that of the CH_2O-T profile in the temperature domain. At x/d=30, the rising branch and the decreasing branch of the JPDF CH-T profiles become closer and start to merge together as the temperature field becomes more uniform downstream, while a rising branch can still be discerned from the JPDF CH-T profiles. Note that the JPDF CH-T distribution at x/d=30, where reactions are rather distributed, is approximately centered on the laminar profile. This, however, is not because of the similarity of the flame structures but rather due to narrow temperature range at downstream locations of the flames.

To better understand the CH-T correlation, simultaneous images of temperature, CH, OH as well as the relative reaction rate $R^*_{CH,c}$ for flames LUPJ10-66 and LUPJ10-418 are shown in Fig.12. To compare different scalars, iso-temperature contours of <T> = 600 K (white curve) and 1300 K (red curve) are shown in the lower images of each flame (x/d<20) , while the upper images (x/d>20) show <T> = 1000 K (white curve) and 1550 K (red curve). The values of red curves were selected based on the most probable temperature for peak CH intensities at different axial locations shown in Fig.10. It can be seen from Fig. 12A that the red curves are closely correlated with the structures in the CH, OH, and $R^*_{CH,c}$ fields for flame LUPJ10-66. The CH layer is in general thin but localized CH signals which are at relatively lower intensity but well-above the detection limit were observed in regions close to the reactant side, being responsible for the rising branch of the JPDF CH-T profile observed from 600 K (cf. Fig.11).

Spatial correlations between these CH signals with the temperature field can be found as exemplified by comparing with the white curves (<T>= 600 K). The broadened CH layer towards the reactant side could not be fully explained by the flame folding from the third dimension as the corresponding temperatures of the CH layer in a laminar flamelet manifold are typically much higher. This observation suggests a possible distortion mechanism of the reaction zone by turbulence even for flames in the TRZ regime, while the reaction zone remains overall thin and the distortion is comparably trifling that may not easily be discerned from noise for many CH PLIF measurements with limited SNRs. Comparing with the flame LUPJ10-66 at 6<x/d<19, the CH layer for flame LUPJ10-418 becomes even more broadened with a slightly different appearance that the CH intensities are less locally concentrated. Similarities between the inner side of the CH layer and the white curve (<T> = 600 K) can still be found while the red curve (<T> = 1300 K) falls in the middle of the broadened CH layer, being less correlated with the structures in both the CH, OH and $R^*_{CH,C}$ fields. At locations downstream (20<x/d<34), the correlation of iso-temperature contours with other scalars, in particular, OH and $R^*_{CH,C}$ appears to be closer.

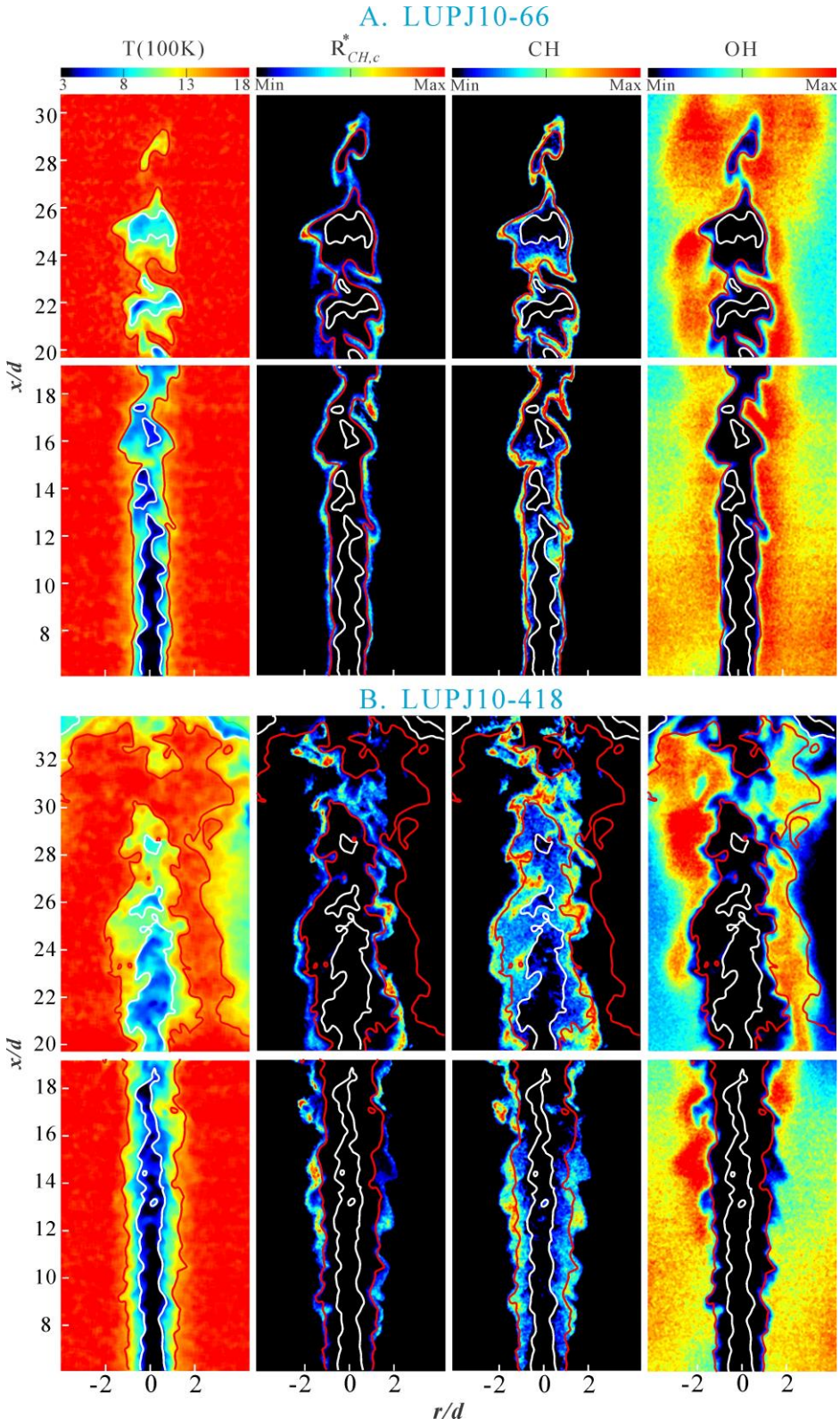

Figure 12. Examples from the T/CH/OH dataset: simultaneous snapshots of scalars (i.e. T, CH and OH), the relative reaction rate $R^*_{CH,c}$ from flames LUPJ10-66 and LUPJ10-418. Iso-temperature contours <T> of 1300 K (red) and 600 K (white) for the lower image of each flame, and of 1550 K (red) and 1000 K (white) for the upper image of each flame were added for comparison.

It is noted that the $R^*_{CH,c}$ layer (see also Fig.5) appears relatively thin in both flames and could be locally broadened but to a less extent compared with CH. Its correlations with temperature for flames LUPJ10-66/220/418 at *x*/d=10, 24, and 30 are characterized by the JPDF plots shown in Fig.13. The red dashed curve represents the $R^*_{CH,c}$-T correlation measured in the laminar flame LUPJ10-11 for comparison. At *x*/d=10, the relative reaction rates $R^*_{CH,c}$ for all flames are consistently lower than the laminar flame counterpart, and flames with higher U_0 give lower peak values of R^*_{CH}, which is associated with the simultaneous reduction of both CH and OH intensities observed at *x*/d=10 with increasing U_0. The $R^*_{CH,c}$-T profiles peak at around 1450 K for LUPJ10-66 and at 1650 K for LUPJ10-418 which are slightly higher than that of their corresponding CH-T profiles. At locations downstream (e.g. *x*/d=24), recovery of the $R^*_{CH,c}$ intensity being comparable with its laminar flame counterpart can be observed, and the peak values of $R^*_{CH,c}$ of the different flames become similar. Similar to the CH-T profiles shown in Fig.11, the $R^*_{CH,c}$-T profiles also exhibit the two branches (i.e., the rising branch and the decreasing branch). As discussed earlier, the Reaction II has a temperature-independent reaction rate constant, and therefore the strength of the relative reaction rate $R^*_{CH,c}$ of the Reaction II is merely proportional to CH and OH concentrations, i.e., put in other terms, to the availability of CH and OH radicals which is implicitly related to temperature through reactions. It is shown that $R^*_{CH,c}$-T profiles are mostly located at the temperature range of 1000 to 1800 K, and contain similar shape in general with the laminar profile regardless of flame conditions. It is noteworthy that the relative probability of finding $R^*_{CH,c}$ signals at a relative low temperature range (T < 1000 K) is not as significant as the probability of finding CH signals at the same temperature range (cf. Fig.11). Associated with this, it is further indicated by JPDFs of T and CH conditioned

on the presence of OH radicals (data not shown) that a noticeable fraction of CH signals does not coexist with OH at the low temperature range, although the enhanced transport of OH radicals to low temperature range with increasing U_0 has been evidenced [24]. This indicates that the increased total amount of OH transported to the low temperature range cannot fully account for the increasingly CH broadening with U_0. It is possible that OH radicals may still be presented with concentrations lower than our detection limit (~ 100ppm), but it also suggests other factors that may take major responsibility for CH production. In fact, chemical analysis using both the GRI mechanism [38] and the Glarborg mechanism [42] indicates that CH production is mostly attributed to the reaction $CH_2+H \rightarrow CH+H_2$. Therefore, the absence of OH radicals at regions where CH radicals are presented with broadening suggests that differential diffusion could still be important even under conditions of high turbulence intensities, leading to different distributions of H and OH radicals. The same implication has also been made in our previous study from the observation of different behaviors of CH and HCO radicals when the flame is partially quenched [24]. Consistent with the experimental findings, recent studies of distributed reactions using direct numerical simulations [46-48] also show that H radicals play a more important role than OH radicals in the DRZ regime for both hydrogen/air and methane/air flames.

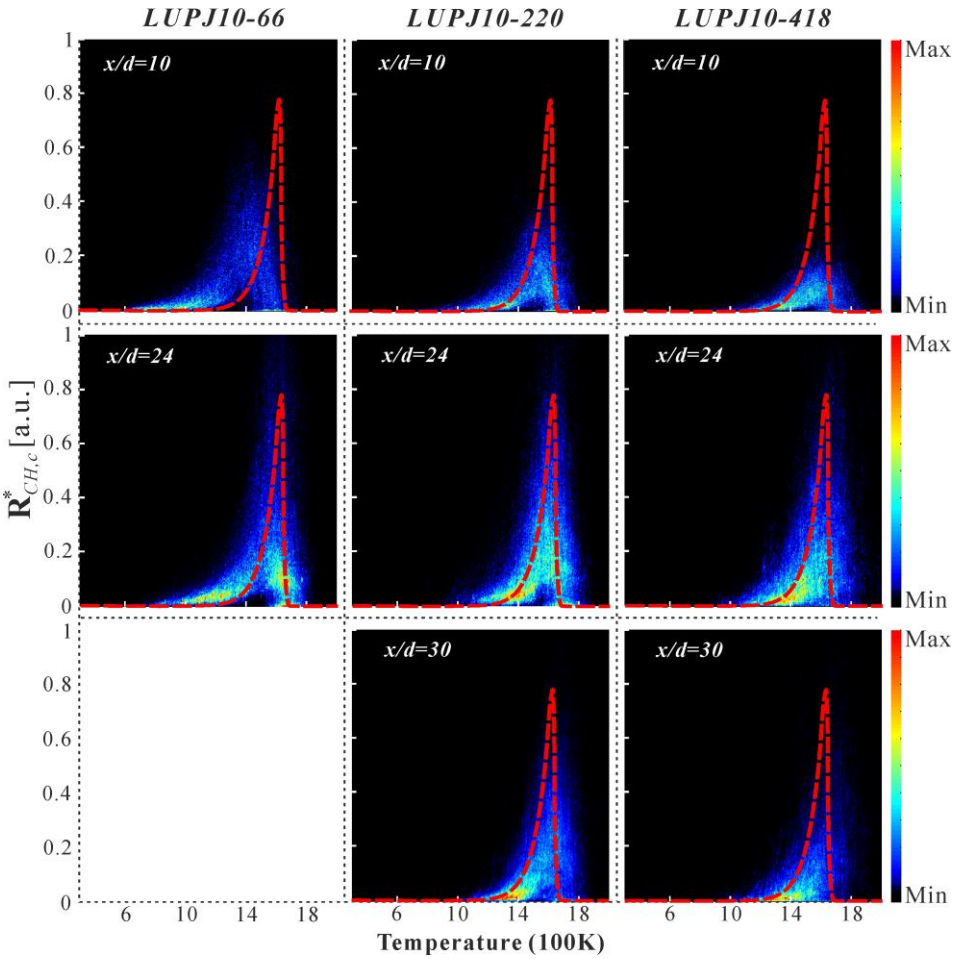

Figure 13. JPDFs of the relative reaction rate $R^*_{CH,c}$ and temperature for the selected flames, the selected flames, LUPJ10-66 (column 1), LUPJ10-220 (column 2) and LUPJ10-418 (column 3) at axial locations of x/d=10, 24 and 30. The red dashed curve represents the $R^*_{CH,c}$-T correlation measured in the laminar flame LUPJ10-11 for comparison.

5.4 Small-scale structures and effect of eddy transport

In this section, small-scale flame structure and the effect of small-scale turbulence on the broadening of the inner layer are examined. Fig.14 (a1-a3) shows the overall flame structure of the flame LUPJ10-110 illustrated by simultaneous CH/CH_2O/OH measurements, and the OH isosurface (10% of the maximum intensity) was superimposed on the measured scalar images for comparison. Associated with the non-flamelet behavior of the flames in the TRZ regime shown earlier in Fig.11 and Fig.12, Fig.14 provides an example of a significant local broadening of the CH layer that has been occasionally observed in flame LUPJ10-110. The local CH

broadening is marked by a square and further displayed in Fig.14 (b1-b3), where significant broadening of the CH layer up to ~ 3 mm is seen. The local CH broadening is so significant that it can hardly be attributed to flame folding from the third dimension. In contrast to a laminar flamelet structure in which the CH layer of ~ 200 μm lies in the thin OH/CH_2O overlapping region [24], Fig.14 (b1-b3) shows that OH and CH_2O barely coexist at regions of strong CH signal. The isosurface of CH (red curve) coincides well with both the edges of high OH and CH_2O signal regions. As indicated by the arrows, the imaged structure resembles the motion of small eddies that roll in CH_2O (and likely other reactants) from the unburned side and bring in OH (and likely other radicals) from the product side. Such turbulence mixing of reactants and radicals occurs rapidly along with chemical reactions including those that generate CH. The process of the mixing has also been reflected in the CH image: on the upper-left of the images of Figs.14 (b1-b2), following the direction of the arrow, the CH_2O signal gradually decreases with a corresponding increase of CH signal as CH_2O is rolling in; a similar correlation between OH and CH signal intensities is also observed following the arrow on the bottom-right of the images in Fig.14 (b1) and (b3). This observation is consistent with the fact that distributed reactions are associated with the penetration of OH radicals (and likely other radicals) into the preheat zone [24, 49]. It appears that the eddy-like structures of OH and CH_2O have a diameter of ~ 3 mm, which is comparably larger than the thickness of the flame front but close to the integral scale in the present flame. This experimental observation seems to support the speculation depicted by Lipatnikov [50] that "*the thickening of the flamelets starts from small-eddy penetration and then larger and larger eddies could penetrate into thicker and thicker reaction zones and thereby broadening them further and further. Due to such a penetration-*

broadening-penetration cascade, the reaction zone could finally reach a thickness of the order of the integral length scale."

Figure 15 (a1-a6) shows an example of CH/CH_2O/OH measurements for the LUPJ10-418 flame in which distributed reactions constantly occur over a wide range in space, and unlike the flamelet structures, CH, OH and CH_2O can here substantially overlap with each other. Examples of local fine structures of distributed reactions in three regions marked by the squares in Fig.15 (a3) and (a6) are displayed in Fig.15 (b-d). Iso-surfaces of the measured scalars are used for illustration of their correlations. As shown in Fig.15 (b-d), local intensity variation of either CH, OH or CH_2O signals even at scales as small as 100 μm can be positively/negatively correlated with the intensity variation of other scalars. First of all, this indicates that the LIF signals of each scalar are qualitatively proportional to its concentrations. Secondly, the correlated structures at small scales should not be considered trivial, as the possibility to accidentally find correlation between three independent measurements is extremely scarce. Nevertheless, in the middle area of Fig.15 (b1-b3) where OH signal levels are low or medium, it can also be noted that there are structures in scalars of e.g. CH and CH_2O on the resolvable scales around 100 μm that could appear chaotic and remain uncorrelated. This indicates that the chemical reactions rather than turbulent mixing become rate-limiting at small scales, especially when the concentrations of reactive radicals are low. The fields of scalars could be even less correlated as the *Ka* further increases. Indications on this trend reported previously [24] in flames with the same jet velocity as LUPJ10-418 but leaner equivalence ratios.

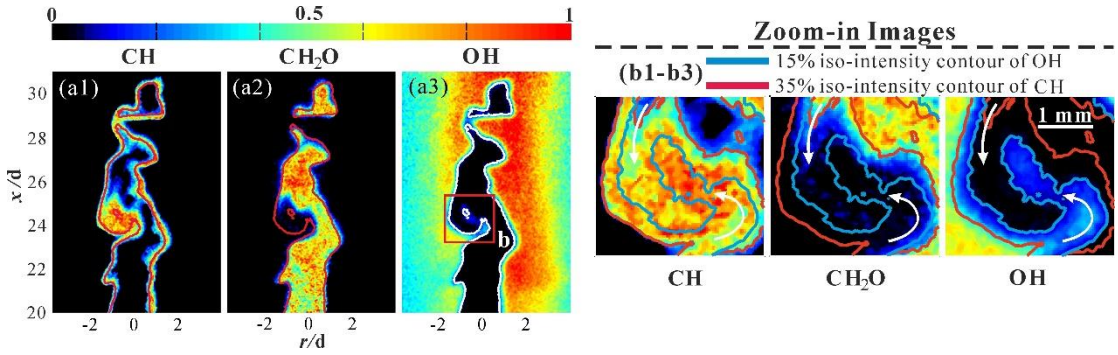

Figure 14. (a1-a3) Overall flame structure for the flame LUPJ10-110 illustrated by simultaneous CH/CH_2O/OH images, featuring overall flamelet-like structure. An OH isosurface (10% of maximum intensity) is superimposed on the image of each scalar for comparison. Detailed flame structures of a local CH broadening identified are further illustrated in the zoom-in images of (b1-b3) together with isosurfaces of the measured scalars to facilitate comparison.

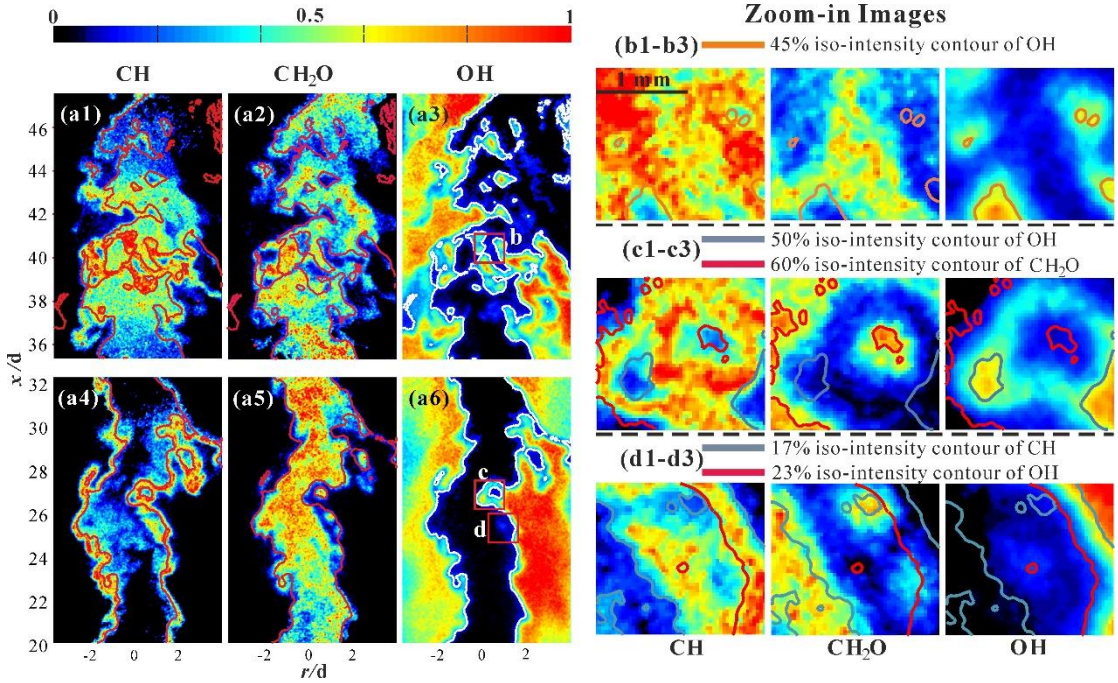

Figure 15. (a1-a6) Overall flame structure for the flame LUPJ10-418 illustrated by simultaneous CH/CH_2O/OH images, featuring distributed reaction combustion. An OH isosurface (20% of maximum intensity) is superimposed on image of each scalar for comparison. Detailed flame structures are further illustrated in the zoom-in images of (b1-b3), (c1-c3) and (d1-d3) together with isosurfaces of the measured scalars to facilitate comparison.

6. Concluding remarks

The present paper reports on experimental studies of a series of turbulent premixed methane/air

flames with varying jet speeds, covering the thin reaction zone (TRZ) regime and the distributed reaction zone (DRZ) regime. Four simultaneous multi-scalar imaging datasets were presented, including combinations of HCO/CH_2O/OH, CH/CH_2O/OH, T/CH_2O/OH and T/CH/OH. The data are analyzed to provide a comprehensive understanding of flame structures in different combustion regimes. Chemical kinetics analysis reveals that both HCO and CH radicals have short lifetimes on the nanosecond scale, which are too short for these radicals to be transported to any appreciable distance away from the reaction zone by turbulence, indicating that observation of distributed HCO and CH zones are direct evidence of distributed reactions. In addition, it appears that the thin CH and HCO layers cannot be directly broadened through small-eddy penetration, while turbulence eddies could transport the relative long-lived radicals such as H and OH from the reaction zone and post-flame zone to the unburned regions reacting with (intermediate) reactants to produce CH and HCO. The onset of distributed CH and HCO zones requires the intermediate species (e.g. CH_3, CH_2, and CH_2O) upstream of CH and HCO in the chemical paths to be distributed first. Associated with the distributed HCO and CH zones observed, the flame structures in the DRZ regime are shown to also feature a significant broadening of the $[OH]_{LIF}\times[CH_2O]_{LIF}$ and filament-like structures in both the $|\nabla T|_{2D}$ and the $|\nabla[OH]|_{2D}$ fields in regions of reactants. Both the $R^*_{HCO,c}$ and $R^*_{CH,c}$ layers appear thin in general and are likewise broadened at localized regions to a less extent. The absolute values of $|\nabla T|_{2D}$ were shown to decrease both along the axial direction and by increasing jet speed, and the mean maximal temperature gradient is shown to be as small as 150 K/mm when distributed reactions prevail comparing with 3000 K/mm obtained in a typical laminar flame.

Other major findings/observations drawn from the correlation analysis of scalars are

summarized in the following:

- Correlation analysis for HCO and $[OH]_{LIF}\times[CH_2O]_{LIF}$ thicknesses suggests that representation of HCO by the $[OH]_{LIF}\times[CH_2O]_{LIF}$ becomes less valid with increasing turbulence intensity and that ambient air entrainment could further deteriorate the correlation.
- Both simultaneous imaging and JPDF analysis show that distributed/broadened CH zones are not always accompanied by the presence of OH radicals. A more important role of turbulent transport of H radicals in realizing distributed reactions is suggested.
- When distributed reactions are prevailing (e.g. at locations downstream of LUPJ10-418), the correlations of temperature with various scalars show that temperature gradients located approximately at from 800 K to 1600 K, CH from 1000 K to 1800 K, and R_{CH}^{*} from 1200 K to 1800 K. A clear shift in the corresponding temperatures of different scalars can be seen. Their correlations with temperature are also shown to be significantly deviated from their laminar counterparts.
- Although the CH layer has been shown to be overall thin for flame LUPJ10-66/110 in the TRZ regime, the CH layer (which could still be seemingly thin) in flame LUPJ10-66 with Ka=25 is shown to also contain parts that protrude into the unburnt regions of lower temperatures. This accounts for the observation from the CH-T JPDFs which show a linear increase of CH signals with temperatures from ~ 600 K to ~ 1500 K followed by a sharp decrease of CH signals at higher temperatures for all flames including LUPJ10-66 in the TRZ regime. This observation suggests that turbulent distortion of the reaction zone could already occur in the TRZ regime to a less extent, although the majority of the reaction zone

is still flamelet-like.

- Instantaneous structures in the fields of both CH, $R^*_{CH,c}$ and OH for flame LUPJ10-66 in the TRZ regime are shown to be able to correlate with a single iso-temperature contour. As for flame LUPJ10-418, iso-temperature contours of various values show only partial correlation with the fields of both CH, $R^*_{CH,c}$ and OH at locations upstream due to strong flame stretch. The correlation of scalars' structures with iso-temperature contour seems to be recovered downstream.
- A possible onset of a local CH layer thickening has been analyzed for flame LUPJ10-110 as a consequence of local rapid turbulent mixing between unburnt reactants (represented by CH_2O) and radicals (represented by OH). As for complete distributed reactions observed in LUPJ10-418, CH, CH_2O and OH are found to be substantially overlapped at small scales. Correlated structures of 100 μm are identified from the correlated intensity variations of scalars at small scales. Uncorrelated structures at resolvable scales have also been observed suggesting chemical reactions rather than turbulent mixing is the rate-limiting process.

Acknowledgements

The authors gratefully acknowledge financial support from VR (Swedish Research Council) and the Swedish Energy Agency through CECOST (Centre for Combustion Science and Technology) and the European Research Council Advanced Grant through the TUCLA program. Bo Zhou thanks Vladimir Alekseev for his support in CHEMKIN simulations.

References

[1] Borghi R. Prog Energy Combust Sci. 14 (1988) 245-92.
[2] Williams FA. Combustion Theory. Second ed. California: The Benjamin/Cummins Publishing Company Inc.; 1985.
[3] Peters N. Proc Combust Inst. 32 (2009) 1-25.
[4] Peters N. Turbulent Combustion. Cambridge: Cambridge University Press; 2000.
[5] Peters N. Proc Combust Inst. 21 (1988) 1231-50.
[6] Pitsch H. Annu Rev Fluid Mech. 38 (2006) 453-82.
[7] Shepherd IG, Cheng RK, Plessing T, Kortschik C, Peters N. Proc Combust Inst. 29 (2002) 1833-40.
[8] de Goey LPH, Plessing T, Hermanns RTE, Peters N. Proc Combust Inst. 30 (2005) 859-66.
[9] Yamamoto K, Isii S, Ohnishi M. Proc Combust Inst. 33 (2011) 1285-92.
[10] Sankaran R, Hawkes ER, Chen JH, Lu TF, Law CK. Proc Combust Inst. 31 (2007) 1291-8.
[11] Poludnenko AY, Oran ES. Combust Flame. 158 (2011) 301-26.
[12] Bell JB, Day MS, Grcar JF. Proc Combust Inst. 29 (2002) 1987-93.
[13] Poinsot T, Veynante D, Candel S. J Fluid Mech. 228 (1991) 561-606.
[14] Gulder OL. Proc Combust Inst. 31 (2007) 1369-75.
[15] Yuen FTC, Gulder OL. Proc Combust Inst. 34 (2013) 1393-400.
[16] Driscoll JF. Prog Energy Combust Sci. 34 (2008) 91-134.
[17] Najm HN, Paul PH, Mueller CJ, Wyckoff PS. Combust Flame. 113 (1998) 312-32.
[18] Vagelopoulos CM, Frank JH. Proc Combust Inst. 30 (2005) 241-9.
[19] Dunn MJ, Masri AR, Bilger RW, Barlow RS, Wang GH. Proc Combust Inst. 32 (2009) 1779-86.
[20] Dunn MJ, Masri AR, Bilger RW, Barlow RS. Flow Turbul Combust. 85 (2010) 621-48.
[21] Arghode VK, Gupta AK, Bryden KM. Appl Energ. 92 (2012) 822-30.
[22] Huang CC, Shy SS, Liu CC, Yan YY. Proc Combust Inst. 31 (2007) 1401-9.
[23] Zhou B, Brackmann C, Li ZS, Alden M, Bai X-S. Proc Combust Inst. 35 (2014) 1409-16.
[24] Zhou B, Brackmann C, Li Q, Wang Z, Petersoon P, Li Z, Alden M, Bai X-S. Combust Flame. 162 (2015) 2937-53.
[25] Zhou B, Li Q, He Y, Pertersson P, ZS.Li, Alden M, Bai XS. Combust Flame. 162 (2015) 2954-8.
[26] Li ZS, Li B, Sun ZW, Bai XS, Alden M. Combust Flame. 157 (2010) 1087-96.
[27] Nikolaou ZM, Swaminathan N. Combust Flame. 161 (2014) 3073-84.
[28] Zhou B, Kiefer J, Zetterberg J, Li ZS, Alden M. Combust Flame. 161 (2014) 1566-74.
[29] Paul PH, Najm HN. Proc Combust Inst. 27 (1998) 43-50.
[30] Fayoux A, Zahringer K, Gicquel O, Rolon JC. Proc Combust Inst. 30 (2005) 251-7.
[31] Gordon RL, Masri AR, Mastorakos E. Combust Theor Model. 13 (2009) 645-70.
[32] Bhagatwala A, Luo ZY, Shen H, Sutton JA, Lu TF, Chen JH. Proc Combust Inst. 35 (2015) 1157-66.
[33] Medwell PR, Kalt PAM, Dally BB. Combust Flame. 148 (2007) 48-61.
[34] Bockle S, Kazenwadel J, Kunzelmann T, Shin DI, Schulz C, Wolfrum J. Proc Combust Inst. 28 (2000) 279-86.
[35] Ayoolan BO, Balachandran R, Frank JH, Mastorakos E, Kaminski CF. Combust Flame. 144 (2006) 1-16.
[36] Balachandran R, Ayoola BO, Kaminski CF, Dowling AP, Mastorakos E. Combust Flame. 143 (2005) 37-55.
[37] Kiefer J, Ossler F, Li ZS, Alden M. Combust Flame. 158 (2011) 583-5.
[38] Gregory P. Smith, David M. Golden, Michael Frenklach, Nigel W. Moriarty, Boris Eiteneer, Mikhail Goldenberg, C. Thomas Bowman, Ronald K. Hanson, Soonho Song, William C. Gardiner, Jr. VVL, Qin Z.

GRI-MECH3.0. http://www.me.berkeley.edu/gri_mech/.
[39] Peters N, Williams FA. Combust Flame. 68 (1987) 185-207.
[40] Seshadri K, Peters N. Combust Flame. 81 (1990) 96-118.
[41] Seshadri K, Bai XS, Pitsch H, Peters N. Combust Flame. 113 (1998) 589-602.
[42] Glarborg P, Alzueta MU, Dam-Johansen K, Miller JA. Combust Flame. 115 (1998) 1-27.
[43] Aaron W. Skiba, Timothy M. Wabel, Jacob E. Temme, F.Driscol J. 54th AIAA Aerospace Sciences Meeting. (2016) 1454.
[44] Aaron W. Skiba, Timothy M. Wabel, Jacob E. Temme, F.Driscol J. 51st AIAA/SAE/ASEE Joint Propulsion Conference. (2015) 4089.
[45] Mansour MS, Peters N, Chen YC. Proc Combust Inst. 27 (1998) 767-73.
[46] H. Carlsson, R.Yu, Bai XS. Proc Combust Inst. (2014) DOI: 10.1016/j.proci.2014.09.002.
[47] Aspden AJ, Day MS, Bell JB. Proc Combust Inst. 35 (2014) 1321-9.
[48] Aspden AJ, Day MS, Bell JB. Proc Combust Inst. 33 (2011) 1463-71.
[49] Carlsson H, Yu RX, Bai XS. Int J Hydrogen Energy. 39 (2014) 20216-32.
[50] Lipatnikov A. Fundamentals of Premixed Turbulent Combustion. New York: CRC Press, Taylor & Francis Group; 2013.